Natural Sunlight-Driven Oxidation of Mn^{2+}(aq) and Heterogeneous Formation of Mn oxides on Hematite

Junyeong Choi[1], Wooyeol Choi[1], Hoyoung Hwang[1], Yuanzhi Tang[2,*] and Haesung Jung[1,*]

[1]Department of Chemical Engineering, Changwon National University, Changwon, Gyeongsangnam-do, 51140, Republic of Korea

[2]School of Earth and Atmospheric Sciences, Georgia Institute of Technology, Atlanta, Georgia, 30332, United States

*Corresponding authors.

Haesung Jung. Email: haesung.jung@changwon.ac.kr; Phone: +82 (55)213-3756

Yuanzhi Tang. Email: yuanzhi.tang@eas.gatech.edu; Phone: +1 (404)894-3814

ABSTRACT

The oxidation of dissolved Mn^{2+}(aq) plays a critical role in driving manganese cycles and regulating the fate of essential elements and contaminants in environmental systems. Based on sluggish oxidation rate, abiotic processes have been considered less effective oxidation pathway for manganese oxidation in environmental systems. Interestingly, a recent study (Jung et al., 2021) has shown that the rapid photochemical oxidation of Mn^{2+}(aq) could be a feasible scenario to uncover the potential significance of abiotic Mn^{2+}(aq) oxidation. Nevertheless, the significance of photochemical oxidation of Mn^{2+}(aq) under natural sunlight exposure remains unclear. Here, we demonstrate the rapid photocatalytic oxidation of Mn^{2+}(aq) and the heterogeneous growth of tunnel-structured Mn oxides under simulated freshwater and seawater conditions in the presence of natural sunlight and hematite. The natural sunlight-driven photocatalytic oxidation of Mn^{2+}(aq) by hematite showed kinetic constants of 1.02 h^{-1} and 0.342 h^{-1} under freshwater and seawater conditions, respectively. The natural sunlight-driven photocatalytic oxidation rates are quite comparable to the results obtained from the previous laboratory test using artificial sunlight, which has ~4.5 times stronger light intensity. It is likely because of ~5.5 times larger light exposure area in the natural sunlight-driven photocatalytic oxidation than that of the laboratory test using artificial sunlight. We also elucidate the roles of cation species in controlling the oxidation rate of Mn^{2+}(aq) and the crystalline structure of Mn oxide products. Specifically, in the presence of large amounts of cations, the oxidation rate of Mn^{2+}(aq) was slower likely because of competitive adsorption. Furthermore, our findings highlight that Mg^{2+} contributes significantly to the formation of large-tunneled Mn oxides. These results illuminate the importance of abiotic photocatalytic processes in controlling the redox chemistry of Mn in real environmental aqueous systems on the oxidation of Mn^{2+}(aq), and provide an environmentally sustainable approach to effectively remediate water contaminated with Mn^{2+}(aq) using natural sunlight.

Keywords:

Dissolved Mn(II), Natural sunlight, Photocatalytic oxidation, Hematite, Mn oxides, Heterogeneous nucleation

1. INTRODUCTION

Manganese (Mn), the tenth abundant element in Earth's crust, is ubiquitous in environmental systems and commonly exists in three oxidation states: Mn(II), Mn(III), and Mn(IV) (Jung et al., 2020; Morgan et al., 2021; Wang et al., 2023). Due to its high reactivity and a broad range of reduction potentials among the three oxidation states, Mn is involved in numerous redox reactions (Spiro et al., 2009; Jung et al., 2020; Wang et al., 2023). Soluble and solid Mn(III/IV) species serve as electron acceptors for microbial anaerobic respiration, and also control the fate and transport of numerous organics, contaminants, and nutrients (e.g., As, Cr, U, Co, Ni, bisphenol A, etc.) (Tebo et al., 2005; Miyata et al., 2007; Brose and James, 2013; Droz et al., 2015; Grebel et al., 2016; Johnson et al., 2016; Balgooyen et al., 2017; Charbonnet et al., 2018; Eitel et al., 2018; Tang et al., 2020; Charbonnet et al., 2021). Thus, understanding the redox pathways of Mn species and the formation mechanisms of Mn(III,IV) (oxyhydr)oxides (hereafter Mn oxides) is of significant interests to biogeochemistry, environmental science and engineering, and materials science (Reinhard et al., 2009; Butterfield et al., 2013; Planavsky et al., 2014; Daye et al., 2019; Huang and Zhang, 2019; Fortunato et al., 2020; Li et al., 2020; Liu et al., 2020; Tang et al., 2020).

The oxidation of Mn^{2+}(aq) and formation of Mn oxides via various abiotic and biotic processes have been extensively studied (Diem and Stumm, 1984; Post, 1999; Spiro et al., 2009; Learman et al., 2011; Wang et al., 2014; Morgan et al., 2021). Under circumneutral pH conditions, the abiotic homogeneous oxidation of Mn^{2+}(aq) by dissolved O_2 takes years (Diem and Stumm, 1984). Heterogeneously catalyzed oxidation of Mn^{2+}(aq) on mineral surfaces (e.g., Fe and Al oxides) can increase the reaction rate to a half-life of 5 to 2,800 days (Sung and Morgan, 1981; Davies and Morgan, 1989; Wehrli et al., 1995). Many studies have shown that microbial oxidation plays a significant role in the natural redox cycles of Mn due to the much faster and environmentally relevant oxidation rates and the ubiquity of microbial processes

(Nealson et al., 1988; Bargar et al., 2005; Spiro et al., 2009; Learman et al., 2011; Butterfield et al., 2013; Madison et al., 2013; Oldham et al., 2016; Toyoda and Tebo, 2016). Consequently, abiotic processes have been generally considered less effective in the oxidation of Mn^{2+}(aq) and formation of Mn oxides in environmental systems. However, recent studies on the photochemical oxidation of Mn^{2+}(aq) showed rapid oxidation rates under the exposure of simulated sunlight (e.g., Xe-lamp and UV lamp), suggesting the previously overlooked abiotic processes also play important roles in natural Mn oxide formation (Anbar and Holland, 1992; Nico et al., 2002; Jung et al., 2017; Zhang et al., 2018; Daye et al., 2019; Jung et al., 2021; Gao et al., 2022). Yet, the effectiveness of natural sunlight in driving this oxidation reaction remain elusive. This is because outdoor experiments are challenging to reproduce due to natural variations, and the photochemical oxidation driven by UV light occurs less effectively under natural sunlight than under simulated light sources (Jung et al., 2017). To investigate the effectiveness of natural sunlight in catalyzing the oxidation of Mn^{2+}(aq), outdoor experiments using realistic sunlight exposure (instead of simulated light source with higher light intensity) are highly desired.

In addition to oxidation rate, the structure of Mn oxides is also an important consideration for comparing different oxidation pathways, as different structured Mn oxides pose different reactivity. Through the abiotic or biotic oxidation of dissolved Mn species, such as Mn^{2+}(aq) and soluble Mn(III)-complex, diverse structures of natural Mn oxides occur in nature. Microbial oxidation, which is generally considered the most effective Mn^{2+}(aq) oxidation process, typically lead to the formation of layer structured Mn(III,IV) oxides, i.e., phyllomanganates such as δ-MnO_2 and birnessite (Bargar et al., 2005; Webb et al., 2006; Spiro et al., 2009). However, abiotic homogeneous and heterogeneous oxidation of Mn^{2+}(aq) showed the formation of only Mn(III) oxides, which are less abundant in oxic environmental systems (Junta and Hochella Jr, 1994; Jun and Martin, 2003; Madden and Hochella, 2005). Recent

studies on abiotic photochemical oxidation of Mn^{2+}(aq) revealed the formation of layer structured Mn(III/IV) oxides, whereas, the photocatalytic oxidation of Mn^{2+}(aq) on mineral surfaces under the exposure of Xe-lamp showed the formation of tunnel structured Mn(III/IV) oxides (tectomanganates), which were not commonly observed in biotic processes (Jung et al., 2021). These studies suggest that understanding the heterogeneous growth of Mn oxides on mineral surfaces in varied aqueous conditions might provide important clues to understanding the polymorphism of natural Mn oxides.

In this study, we investigated the abiotic photocatalytic oxidation of Mn^{2+}(aq) by hematite, which is the most ubiquitous semiconducting mineral and frequently occurs with natural Mn oxides (Burns and Burns, 1977; Chan et al., 2000; Lee and Xu, 2016), in the presence of natural sunlight and in artificial freshwater (AFW) or artificial seawater (ASW) conditions. We show that this is a rapid process leading to the formation of tunnel structured Mn(III/IV) oxides through heterogeneous nucleation on hematite. We also explored the effects of cation species and concentration on the oxidation rate and morphologies of Mn oxide products, further enhancing our understanding of this complex process.

2. MATERIALS AND METHODS

2.1. Materials and reagents.

Hematite nanoparticles were synthesized using a previously established procedure (Cornell and Schwertmann, 2003). X-ray diffraction (XRD, SmartlabSE, Rigaku) and field emission transmission electron microscopy (FE-TEM, JEM 2100F, Jeol) confirmed the formation of ~7 nm hematite nanoparticles (Fig. S1). To simulate the natural sunlight-driven photocatalytic oxidation of Mn^{2+}(aq) by hematite in freshwater and seawater conditions, ASW and AFW were prepared. ASW contained 420 mM NaCl, 25 mM $MgSO_4$, 9.1 mM $CaCl_2$, 8.9 mM KCl, and 2.4 mM $NaHCO_3$ in deionized (DI) water (Montserrat et al., 2017). AFW

contained 0.044 mM $NaNO_3$, 0.448 mM $MgSO_4$, 1.75 mM $CaCl_2$, 0.0623 mM $KHCO_3$, 0.0403 mM KNO_3, and 1.1 mM $NaHCO_3$ in DI water (Ferris et al., 2004). The pH of ASW and AFW was 8.0 ± 0.1 and 7.6 ± 0.1, respectively, which remained stable throughout the experiments. To evaluate the impact of different cation species on the oxidation rate and final products, experiments were also conducted with Na^+, Mg^{2+}, or Ca^{2+} at 10, 34, or 100 mM, each with 2 mM $NaHCO_3$ background electrolyte. The initial pH was adjusted to 8.0 ± 0.1, which remained stable throughout the reactions.

2.2. Photocatalytic oxidation of Mn^{2+}(aq).

To prepare for the experiments, 0.10 g L^{-1} of hematite nanoparticles was suspended in 50 mL of ASW or AFW and dispersed by sonication. We then added $MnCl_2$ to the suspension to obtain 100 μM Mn^{2+}(aq). The photoreactions were conducted in a 100 ml glass flask (light exposed area on 50 ml solutions: ~63.4 cm^2) with continuous stirring. Photocatalytic reactivity of the hematite nanoparticles in ASW or AFW was measured by sequential additions of 100 μM Mn^{2+}(aq) to the suspensions at 0, 3, 6, 12, and 21 hr of the experiments. These time intervals were determined based on the near complete removal of Mn^{2+}(aq). The outdoor photocatalytic reactions were conducted during sunny days in the summer of 2022, between 10 am to 5 pm, on the rooftop of the 2nd engineering building at Changwon National University (Changwon, Gyeongsangnam-do, South Korea 35.2° latitude). The outdoor temperature during the experiments was approximately 29.3 ± 3.6 °C, and the intensity of natural sunlight was measured to be 83 ± 10 mW/cm^2 taken on different dates and reaction times using a photometer (Power Meter Model 843-R, Newport). The photochemical reaction was initiated by exposing the prepared suspensions to the sunlight. To conduct the photocatalytic reaction for more than 7 hours, the reactor was wrapped in aluminum foil and stored in a refrigerator at 4.0 °C overnight after the daytime reaction was completed. The experiment was then resumed the

following day. A dark control experiment was performed by covering the reactor with aluminum foil.

Aliquots of the reaction suspension was collected periodically to analyze the concentration of Mn(III,IV) and dissolved Mn^{2+}(aq) using a UV-Vis spectrophotometer (Cary 60, Agilent) (Jung et al., 2021). Dissolved Mn^{2+}(aq) was measured using the porphyrin colorimetric method at 468 nm (Madison et al., 2011). Mn(III,IV) concentration was analyzed using the leucoberbelin blue (LBB) colorimetric assay at 625 nm (Tebo et al., 2007). The reacted suspensions were mixed with LBB in a 1 to 5 volume ratio, and this reagent exclusively reacts with Mn(III/IV) oxides on hematite, showing no reactivity towards Mn(II) or Fe species. The LBB method uses $KMn^{VII}O_4$ for standard calibration, and 1 mole of Mn(VII) oxidizes 5 moles of LBB, i.e., 1 mole of oxidized LBB equals 1/5 mole of Mn(II) oxidation to Mn(VII). Here, we use Mn(III) equivalent to quantify the amount of transferred electrons via photocatalytic oxidation of Mn^{2+}(aq), i.e., 1 mole of oxidized LBB equals 1 mole of Mn(II) oxidation to Mn(III). At the end of experiments, solid products were collected using sequential centrifugation, washed by DI water three times, and freeze-dried. The freeze-drying process does not result in the structural change of the Mn oxide products (Yang and Xu, 2003; Hjorth, 2004).

2.3. Solid state analyses.

The oxidation state, structure, and morphology of the Mn oxide products were characterized using X-ray photoelectron microscopy (XPS), synchrotron X-ray diffraction (SXRD), scanning electron microscopy (SEM), and transmission electron microscopy (TEM). XPS analysis (Sigma probe, Thermo Fisher Scientific) used C 1s spectrum (284.8 eV) for energy calibration. Mn 3p spectra were collected, as they show better sensitivity than Mn 2p and 3s spectra (Cerrato et al., 2010; Cerrato et al., 2011; Jung et al., 2021). Spectra fitting used

154 the peak positions of 47.8, 48.6, and 49.7 eV for Mn(II), Mn(III), and Mn(IV), respectively,
155 based on the measurement of $Mn^{II}O$, $Mn^{III}OOH$, and β-$Mn^{IV}O_2$ (Fig. S2) and literature data on
156 Mn 3p analyses (Table S1). Following a previous study on Mn 3p spectrum curve fitting, an
157 asymmetric Gaussian-Lorentzian algorithm was applied by granting degrees of freedom to the
158 tail mix in Mn 3p spectrum fitting of more than 80% (Cerrato et al., 2010; Cerrato et al., 2011).
159 SXRD data was collected at Beamline 17-BM at the Advanced Photon Source (APS) at
160 Argonne National Laboratory (Lemont, IL, USA) with a wavelength of 0.45175 Å. The
161 morphology and structure of the Mn oxides was characterized using high resolution field
162 emission SEM (FE-SEM, JSM-7900F, Jeol) operated at 15 kV for Pt coated samples. Field
163 Emission TEM (FE-TEM, JEM 2100F, Jeol) was used to analyze the crystalline structure of
164 nucleated Mn oxide and the interface between Mn oxide and hematite. The samples were
165 placed onto a formvar carbon-coated copper grid. The specific surface areas of hematite in
166 ASW and AFW are measured by using Brunauer-Emmett-Teller (BET) method with N_2 gas
167 adsorption (BELSORP-mini, MicrotracBEL, Japan).
168
169 **3. RESULTS and DISCUSSION**
170 **3.1. Natural sunlight induces rapid photocatalytic oxidation of Mn^{2+}(aq) by hematite.**
171 Natural sunlight induced rapid photocatalytic oxidation of Mn^{2+}(aq) in both ASW-
172 hematite and AFW-hematite suspensions (Fig. 1). Our outdoor sunlight experiments exhibited
173 highly consistent results, displaying narrow error bars with more than four replicate
174 experiments for both ASW-hematite and AFW-hematite reactions (Fig. 1A and 1B). Assuming
175 a pseudo first-order elemental reaction, commonly employed for the kinetic analyses of abiotic
176 oxidation of Mn^{2+}(aq), we obtained the oxidation rates in the ASW-hematite and AFW-
177 hematite suspensions under sunlight exposure (Equations 1 and 2) (Von Langen et al., 1997;
178 Morgan, 2005).

$$\frac{d[Mn(III)]}{dt} = -\frac{d[Mn^{2+}(aq)]}{dt} = k[Mn^{2+}(aq)] \quad (1)$$

$$[Mn^{2+}(aq)] = [Mn^{2+}(aq)]_0 e^{-kt} \quad (2)$$

Here, k is a kinetic constant (h^{-1}), $[Mn^{2+}(aq)]_0$ is the initial concentration of Mn^{2+}(aq), and t is the reaction time. The kinetic analysis revealed that the kinetic constants were 1.02 ± 0.08 h^{-1} and 0.342 ± 0.08 h^{-1} for AFW-hematite and ASW-hematite conditions at pH ~8, respectively (Fig. S3). Notably, the oxidation rate of the hematite-AFW suspension was approximately twice as fast as that of the hematite-ASW suspension (Fig. 1A). The difference might occur from the discrepancy in pH, ionic strength, competitive adsorption of cations, and active surface area of hematite in ASW (164 m^2 g^{-1}) and in AFW (202 m^2 g^{-1}) (Table S2). In contrast, dark control experiments (hematite and Mn^{2+} only, no sunlight) showed minimal oxidation of Mn^{2+} (Fig. 1A and 1B). Also, there was no oxidation of Mn^{2+}(aq) without hematite under natural sunlight (Fig. S4). There is a possibility that the nucleated Mn oxides by the photocatalytic oxidation of Mn^{2+}(aq) on hematite can result in the oxidation of Mn^{2+}(aq) via heterogeneous oxidation on the surface using dissolved oxygen as an oxidation agent and comproportionation-disproportionation. The heterogeneous oxidation of Mn^{2+}(aq) on Mn oxide is considered a much slower reaction based on previous studies than that observed in this study. Considering the kinetic constants (9.6 M^{-1} h^{-1}) of heterogeneous oxidation of Mn^{2+}(aq) by Mn oxide in the previous study, the oxidation rate normalized by 0.1 g/L Mn oxide and 100 μM Mn^{2+}(aq) is 1.1 μM h^{-1}, which is much slower than that observed in this study (> 30 μM h^{-1}) (Diem and Stumm, 1984). For the comproportionation-disproportionation (Mn(IV) + Mn(II) → 2Mn(III)), since the summation of oxidation states are the same before and after the reaction, it does not contribute to the analysis of the oxidized amount of Mn(III) using LBB colorimetric method. Thus, we can infer that the oxidation of Mn^{2+}(aq) by the nucleated Mn oxides is likely much less effective than that of the natural sunlight-driven photocatalytic reaction.

Based on the observed rapid photocatalytic oxidation of Mn^{2+}(aq), we further conducted sequential Mn^{2+}(aq) spiking experiments to assess the photocatalytic reactivity of hematite. The ASW- or AFW-hematite suspensions were spiked with 100 μM Mn^{2+}(aq) multiple times. Results show that 0.10 g L^{-1} (= 625 μM) of hematite oxidizes Mn^{2+}(aq) rapidly over the four spiking periods (i.e., total 400 μM Mn^{2+}(aq)) in both the AFW-hematite and ASW-hematite suspensions. After the first spike (Fig. 1C), the concentration of Mn^{2+}(aq) quickly decreases by 80% in 3 h in the ASW-hematite suspension and over 95% in 3 h in the AFW-hematite suspension. In both the ASW-hematite and AFW-hematite suspensions, the first and second spikes show similar oxidation rates, while the third and fourth spikes showed decreased reaction rates (Table S3). The oxidation becomes much slower after the fifth spike, indicating that the photocatalytic reactivity of 0.10 g L^{-1} hematite is ~400 μM Mn^{2+}(aq). These results could be attributed to factors such as the passivation of the hematite surface due to the deposition of Mn oxides.

3.2. The formation of tunneled Mn(III/IV) oxides via natural sunlight.

Photocatalytic oxidation leads to the formation of Mn(III/IV) oxides on the surface of hematite in both the AFW- and ASW-hematite suspensions. By deconvoluting the Mn 3p XPS spectra, we obtained the average oxidation states (AOS) of the nucleated Mn oxides on hematite (Fig. 2)., To enhance the statistical reliability of the data, we obtained the averages and derivations of each oxidation state based on the XPS analyses for duplicated samples (Table S4). For Mn oxides produced from the first Mn^{2+}(aq) spike, the AOS is 2.90 and 3.17 for the AFW- and ASW-hematite suspensions, respectively. Both conditions show percentages of Mn(II) contribution, likely from the adsorption of Mn^{2+}(aq) on hematite and the pre-formed Mn oxides. The AOS of Mn oxides resulting from natural sunlight-driven photocatalysis by hematite in ASW in this study is similar to that obtained with Xe lamp (AOS 2.91, Mn(II) 35 %,

228 Mn(III) 39 %, and Mn(IV) 26%) in our previous study (Jung et al., 2021).

229 Interestingly, Mn oxides obtained from five spikes of Mn^{2+}(aq) showed significant
230 differences in AOS depending on the solution conditions. The AOS of Mn oxides formed in
231 the AFW- and ASW-hematite suspensions after fifth spikes are 3.34 and 3.76, respectively. Mn
232 oxides from the AFW-hematite suspension showed much higher proportion of Mn(IV) (78%)
233 and lower proportion of Mn(II) (2%) compared to that from the ASW-hematite suspension
234 (Mn(IV) 42%, Mn(II) 18%).

235 We further identified the formation of tunnel structured Mn(III/IV) oxides in both the
236 AFW- and ASW-hematite suspensions. SXRD showed weak diffractions of poorly crystalline
237 Mn oxides with hematite (Fig. 3). In the ASW-hematite suspension, the diffractions at ~5.8 Å
238 and ~3.9 Å (Fig. 3A) newly occurred. While it is challenging to clearly identify the structure
239 of minerals using the two diffraction peaks, of all known Mn(III/IV) oxide phases, only
240 romanechite (2 × 3 tunnel structure) exhibits the diffractions at ~5.8 Å ($\bar{2}$01) and ~3.9 Å (202)
241 (Jung et al., 2021).

242 In contrast, in the AFW-hematite suspension, we observed diffractions only from
243 hematite and a weak and broad diffraction (i.e., amorphous-like structure) at ~4.8 Å (Fig. 3B).
244 This diffraction occurs from most large tunnel-structured Mn oxides, such as romanechite,
245 todorokite, cryptomelane (α-MnO_2), and hollandite. This weak diffraction indicates that the
246 nucleated Mn oxide in the AFW-hematite suspension also has a $n \times m$ large tunneled (n & $m \geq$
247 2) structure, but the crystallinity or amount might be too low to be identified by SXRD.

248 We used SEM and TEM to confirm the morphological and structural images of the
249 nucleated Mn oxide on hematite nanoparticles. SEM revealed the occurrence of poorly
250 crystalline spherical-shaped Mn oxide nanoparticles and well-structured nanorods on hematite
251 in the ASW- and AFW-hematite suspensions, respectively (Fig. 4A–4C). In the ASW-hematite
252 suspension, compared to pristine hematite nanoparticles (Fig. 4A), we found no significant

253 difference in the morphology of the nucleated Mn oxides from hematite nanoparticles (Fig.
254 4B). However, in the AFW-hematite suspension, the formation of nanorods clearly shows the
255 morphological difference from the hematite nanoparticles (Fig. 4C). The images of elemental
256 mapping using TEM energy-dispersive X-ray spectroscopy (TEM-EDS) showed that the
257 overlap of Fe and Mn from the aggregated nanoparticles in the ASW-hematite suspension (Fig.
258 S5). In the AFW-hematite suspension, while the overlap of Fe and Mn occurred from the
259 aggregated nanoparticles, the nanorods contained only Mn (Fig. S5).

260 We employed high-resolution TEM (HRTEM) to gain deep insights into the crystalline
261 structure of Mn oxides (Fig. 4). We were able to identify crystalline nanoparticles that were
262 distinguishable from the well-crystalline hematite nanoparticles (Fig. 4E). These crystalline
263 nanoparticles exhibited d-spacings of 9.6 and 2.4 Å (Fig. 4F). The d-spacing of 9.6 Å is not
264 characteristic of hematite, suggesting that the observed nanoparticles originate from nucleated
265 Mn oxide. Moreover, the angle (~60˚) observed from the FFT between 9.6 Å (001) and 2.4 Å
266 (112) is well-matched with only romanechite (monoclinic, a = 13.929 Å, b = 2.8459 Å, c =
267 9.678 Å, β = 92.39°) (Fig. 4F) (Turner and Post, 1988). Therefore, our TEM and XRD analyses
268 support the formation of romanechite in the ASW-hematite suspension. Our finding not only
269 corroborates the previous research which revealed that romanechite can form through
270 simulated sunlight-driven photocatalytic oxidation of Mn^{2+}(aq) in the ASW-suspension (Jung
271 et al., 2021), but also provides additional information regarding the morphology and crystalline
272 structure of the nucleated romanechite on hematite.

273 In the AFW-suspension, TEM analysis identified the formation of todorokite (3 × 3
274 tunnel structured Mn(III/IV) oxide) (Fig. 4H and 4I). The Mn oxide nanorods formed in the
275 AFW-hematite suspension have the d-spacings of 4.9 Å and 3.2 Å, and an angle between the
276 d-spacings of ~90˚ (Fig. 4I). While other large tunnel structured Mn(III/IV) oxides have similar
277 d-spacings, the angle between 4.9 Å (002) and 3.2 Å (300) is exclusive to todorokite. FFT-ED

(Fig. 4I) clearly shows (200), (003) and (203), all of which occur from [060] zone axis of todorokite. Taken together, our findings show that the nucleated Mn oxides on the surface of hematite are large tunnel structured Mn oxides. The formation of these tunnel structures (romanechite and todorokite) is attributed to the surface of hematite serving as templates for heterogeneous nucleation (Jung et al., 2021). Furthermore, the observed differences between the AFW- and ASW-hematite reactions suggest that cations and ionic strengths might play a critical role not only in the oxidation kinetics but also in the structure and crystallinity of the Mn oxide products.

3.3. The important roles of cations in the photocatalytic oxidation of Mn^{2+}(aq).

To explain the observed differences in the oxidation kinetics and crystalline structures between the ASW- and AFW-hematite suspensions, we investigated the role of single cation species and concentration. Considering that Mg^{2+}, Ca^{2+}, and Na^{+} are the major cations of differences between ASW and AFW, we conducted photocatalytic oxidation of Mn^{2+}(aq) under varied concentrations of 10, 34 and 100 mM for each cation species (Fig. S6). Interestingly, our kinetic analysis revealed that both cation species and concentration significantly affect the oxidation rate. Compared to Mg^{2+} and Na^{+}, the presence of Ca^{2+} resulted in much slower oxidation than that in AFW-hematite and ASW-hematite suspensions (Table S5), suggesting that the contribution of Ca^{2+} on the photocatalytic oxidation in both the AFW- and the ASW-hematite suspensions is less significant than the presence of Mg^{2+} and/or Na^{+}. For Mg^{2+} or Na^{+}, we observed a distinctively lower oxidation rate at 100 mM compared to 10 and 34 mM (Fig. 5A and 5B), suggesting that the high concentration of cations in the ASW-hematite suspension may be responsible for the lower oxidation of Mn^{2+}(aq) than the AFW-hematite condition (Fig. 1A).

In addition, cation species and concentration also influence the morphology of the

nucleated Mn oxides, with nanorods and nanoparticles occurring with different cation species and concentrations (Fig. S7). Interestingly, nanorods occurred only at 10 mM of Na^+ and Mg^{2+} (Fig. 5D and 5E), whereas in other experimental conditions we observed only nanoparticles. Recall that nanorods and nanoparticles occurred in the AFW- and ASW-suspensions, respectively (Fig. 4). The cations were behaved likely as impurities in the adsorption of Mn^{2+}(aq) on the surface of hematite and the formation of Mn oxides. Thus, the slower kinetics and morphological variation might occur at the higher concentrations of cations (De Yoreo and Vekilov, 2003). Moreover, from the analysis of XPS survey scan, we observed the considerable amounts of Na^+, Mg^{2+}, and Ca^{2+} are adsorbed on the surface of reacted hematite is ASW solution, but not in AFW solution (Fig. S8). Notably, despite Mg^{2+} being present in the solution at a concentration 16.8 times lower than that of Na^+, the adsorbed amount of Mg^{2+}(5.23 %) and Na^+(7.06 %) are in similar proportions. In addition, it is well-known that the large tunnel-structured Mn oxide (i.e., todorokite) occurs by Mg^{2+} which works as a framework of the tunnel (Feng et al., 2015; Yuan et al., 2019; Jung et al., 2020). Considering the observed kinetics, morphologies and cation adsorptions, we can infer that the adsorption of Mg^{2+} dominantly affects the competitive adsorption against Mn^{2+}(aq) and the formation of Mn oxides.

3.4. Comparison of the kinetics of Mn^{2+}(aq) oxidation processes in aqueous environments.

This study demonstrates rapid photocatalytic oxidation of Mn^{2+}(aq) by hematite and natural sunlight. We revisited our previous data for the photocatalytic oxidation of Mn^{2+}(aq) in ASW-hematite suspension under 450 W Xe-lamp exposure, and obtained $k = 0.244 \pm 0.01$ h^{-1} (Fig. S9) (Jung et al., 2021). Despite the 450 W Xe-lamp (374 ± 10 mW/cm^2) having approximately 4.5 times higher intensity than natural sunlight (83 ± 10 mW/cm^2), the exposure of natural sunlight resulted in higher or comparable oxidation rates ($k = 0.342 \pm 0.08$ h^{-1}) (Fig. S3) compared to the Xe-lamp (Jung et al., 2021). This similarity in oxidation rates obtained

328 from natural sunlight and the Xe-lamp can be attributed to the ~5.5 times larger area of light
329 exposure in the outdoor experiment (63.4 cm^2) compared to the laboratory test using the Xe-
330 lamp (11.4 cm^2).

331 Using the obtained kinetic constants of the natural sunlight driven photocatalytic
332 oxidation in this study (Equation 2), biotic oxidations (i.e., the Michaelis-Menten (M-M)
333 enzyme kinetics; Equation 3), and abiotic heterogeneous oxidations (Equation 4) , we
334 calculated the oxidation rates of Mn^{2+}(aq) at pH ~8 as the function of $[Mn^{2+}(aq)]_0$ (Fig. 6)
335 (Diem and Stumm, 1984; Toyoda and Tebo, 2016).

336 $$\frac{d[Mn(III)]}{dt} = \frac{-d[Mn^{2+}(aq)]}{dt} = V_{max}[Mn^{2+}(aq)]/(K_m + [Mn^{2+}(aq)]) \quad (3)$$

337 $$\frac{d[Mn(II)]}{dt} = k_1[Mn^{2+}(aq)] + k_2[Mn^{2+}(aq)][MnO_x] \quad (4)$$

338 Here, K_m is a constant related to the active sites of microbes, and V_{max} is the maximum rate of
339 the oxidation of Mn^{2+}(aq). In Equation (4), k_1 and k_2 are kinetic constants of homogeneous
340 oxidation and heterogeneous oxidation on a foreign mineral surface (e.g., MnO_2) by dissolved
341 oxygen (DO), respectively (Diem and Stumm, 1984). We took the values of the parameters
342 based on the previous studies (Table S6 and S7). To accommodate the variation of oxidation
343 rates in biotic processes, we applied conditions obtained from previous studies on microbial
344 oxidation, including the fastest conditions (50 mM NaCl and 10 mM $CaCl_2$) and the slowest
345 conditions (natural seawater), as well as parameters obtained from ASW solution at the
346 representative spore concentration (i.e., 30 mg/L), obtained from previously applied values of
347 spore concentration (5×10^9 spore/L and 1.3×10^8 spore/milligram), for the calculation of
348 oxidation rates (Table S6) (Toyoda and Tebo, 2016). Thus, the range of the calculated microbial
349 oxidation rates as a function of $[Mn^{2+}(aq)]_0$ is in the slashed area (Fig. 6). In addition, the
350 range of light exposure area between 11.4 cm^2 and 63.4 cm^2, which were applied under Xe-
351 lamp and natural sunlight conditions, respectively, was considered as well (Fig. S10). Although

we accommodated the range of oxidation rates under the varied conditions, it is noteworthy that variable parameters, such as microbe concentrations, the area of light exposure, etc., should result in great differences in the oxidation rates. Therefore, the direct comparison of the oxidation rates among the biotic and abiotic processes is limited. Nevertheless, we can infer that the abiotic photochemical reaction is a feasible scenario of the oxidation of Mn^{2+}(aq), not competing with biotic processes, under wide variety of environmental systems with natural sunlight and Fe oxides. Additionally, we normalized the kinetic constants by dividing them by exposure area (cm^2), light intensity (mW/cm^2), and concentration of hematite (g/L) to facilitate comparison of kinetic constants with other photocatalytic manganese oxidations (Table S8). As shown in Fig. 6, previous abiotic oxidation of Mn^{2+}(aq) (homogeneous and heterogeneous oxidation by DO under dark condition) shows orders of magnitude slower oxidation rate than biotic process at a lower concentration of Mn^{2+}(aq) (< 5 μM). However, natural sunlight-driven abiotic photocatalytic oxidation by hematite in this study shows comparable or even much higher oxidation rate than the biotic processes (Fig. 6). Specifically, both sunlight-driven photocatalytic process and biotic process show comparable rate at low Mn^{2+}(aq) concentrations (< 5 μM). Considering that the occurrence of relatively low concentration of Mn^{2+}(aq) in most common environmental aqueous systems, this suggest that abiotic photocatalytic oxidation by natural abundant semiconducting minerals might play a significant role in the natural oxidation of Mn^{2+}(aq) and subsequent formation of diverse structures of Mn oxides.

At higher concentrations of Mn^{2+}(aq), natural sunlight-driven photocatalytic oxidation shows orders of magnitude higher oxidation rate than that of biotic process. The rapid photocatalytic oxidation in the presence of high Mn^{2+}(aq) concentration might bring insights for the remediation of Mn^{2+}(aq)-contaminated sites, such as acid mine drainage and locally contaminated groundwater sites (Chaput et al., 2015; Gillispie et al., 2016). In addition to the high oxidation rate, the high capacity of hematite nanoparticle for the photocatalytic removal

of Mn^{2+}(aq) (Fig. 1C) might be considered for the selection of photocatalytic substrates for Mn^{2+}(aq) remediation. Considering the environmental abundance of hematite, this sunlight driven-process might be a more energy efficient and environmentally friendly alternative for the removal of Mn^{2+}(aq) compared to conventional remediation processes (e.g., lime, permanganate, chlorine, and filter media) (Knocke et al., 1987; Knocke et al., 1988; Knocke et al., 1991).

4. CONCLUSIONS

In this study, we demonstrate the significance of abiotic photocatalytic processes in the oxidation of Mn^{2+}(aq) and the subsequent formation of tunnel-structured Mn oxides under natural sunlight exposure. By investigating simulated freshwater and seawater conditions in the presence of hematite, we reveal the rapid photocatalytic oxidation of Mn^{2+}(aq) and the heterogenous nucleation of Mn oxides. Furthermore, we uncover the influential role of cation species in controlling the photocatalytic oxidation rate of Mn^{2+}(aq) and the crystalline structure of the resulting Mn oxide products. These findings not only emphasize the importance of abiotic photocatalytic processes in the redox chemistry of Mn within environmental aqueous systems but also offer a more environmentally sustainable and energy efficient approach for the effective remediation of Mn^{2+}(aq)-contaminated aquatic systems. Furthermore, these results can help explain the abundance of Mn oxides found with hematite in nature (Burns and Burns, 1977; Chan et al., 2000; Lee and Xu, 2016).

Acknowledgments

This work is supported by the National Research Foundation of Korea (NRF) grant funded by the Korea government (No. 2021R1F1A1063426) and by Changwon National University's Financial Program for Self-Directed Research Capacity in 2022. Y.T. acknowledges support

from the US National Aeronautics and Space Administration (NASA) Grant #80NSSC21K0483 and National Science Foundation (NSF) Grant #2108688. We thank beamline scientists at beamlines 17-BM-B at Advanced Photon Source (APS), Argonne National Laborotary. Use of APS is supported by the U.S. Department of Energy, Office of Science, Office of Basic Energy Sciences, under Contract No. DE-AC02-06CH11357.

Appendix A. Supplementary materials

Supplementary data to this article can be found online at

Declaration of interests

The authors declare that they have no known competing financial interests or personal relatioships that could have appeared to influence the work reported in this paper.

References

Anbar, A.D., Holland, H., 1992. The photochemistry of manganese and the origin of banded iron formations. Geochim. Cosmochim. Acta 56, 2595-2603.

Balgooyen, S., Alaimo, P.J., Remucal, C.K., Ginder-Vogel, M., 2017. Structural transformation of MnO_2 during the oxidation of bisphenol A. Environ. Sci. Technol. 51, 6053-6062.

Bargar, J.R., Tebo, B.M., Bergmann, U., Webb, S.M., Glatzel, P., Chiu, V.Q., Villalobos, M., 2005. Biotic and abiotic products of Mn (II) oxidation by spores of the marine Bacillus sp. strain SG-1. Am. Mineral. 90, 143-154.

Brose, D.A., James, B.R., 2013. Hexavalent Chromium Reduction by Tartaric Acid and Isopropyl Alcohol in Mid-Atlantic Soils and the Role of Mn (III, IV)(hydr) oxides. Environ. Sci. Technol. 47, 12985-12991.

Burns, R.G., Burns, V.M., 1977. Chapter 7 Mineralogy. in: Glasby, G.P. (Ed.). Elsevier Oceanography Series. Elsevier, pp. 185-248.

Butterfield, C.N., Soldatova, A.V., Lee, S.-W., Spiro, T.G., Tebo, B.M., 2013. Mn (II, III) oxidation and MnO_2 mineralization by an expressed bacterial multicopper oxidase. Proc. Natl. Acad. Sci. 110, 11731-11735.

Cerrato, J.M., Hochella Jr, M.F., Knocke, W.R., Dietrich, A.M., Cromer, T.F., 2010. Use of XPS to identify the oxidation state of Mn in solid surfaces of filtration media oxide samples from drinking water treatment plants. Environ. Sci. Technol. 44, 5881-5886.

Cerrato, J.M., Knocke, W.R., Hochella, M.F., Dietrich, A.M., Jones, A., Cromer, T.F., 2011. Application of XPS and Solution Chemistry Analyses to Investigate Soluble Manganese Removal by MnOx(s)-Coated Media. Environ. Sci. Technol. 45, 10068-10074.

Chan, M.A., Parry, W.T., Bowman, J.R., 2000. Diagenetic Hematite and Manganese Oxides and Fault-Related Fluid Flow in Jurassic Sandstones, Southeastern Utah. Am. Assoc. Pet. Geol. Bull. 84, 1281-1310.
Chaput, D.L., Hansel, C.M., Burgos, W.D., Santelli, C.M., 2015. Profiling microbial communities in manganese remediation systems treating coal mine drainage. Appl. Environ. Microbiol. 81, 2189-2198.
Charbonnet, J.A., Duan, Y., van Genuchten, C.M., Sedlak, D.L., 2018. Chemical Regeneration of Manganese Oxide-Coated Sand for Oxidation of Organic Stormwater Contaminants. Environ. Sci. Technol. 52, 10728-10736.
Charbonnet, J.A., Duan, Y., van Genuchten, C.M., Sedlak, D.L., 2021. Regenerated Manganese-Oxide Coated Sands: The Role of Mineral Phase in Organic Contaminant Reactivity. Environ. Sci. Technol. 55, 5282-5290.
Cornell, R.M., Schwertmann, U., 2003. The iron oxides: structure, properties, reactions, occurrences, and uses. Wiley-vch Weinheim.
Davies, S.H., Morgan, J.J., 1989. Manganese (II) oxidation kinetics on metal oxide surfaces. J. Colloid Interface Sci. 129, 63-77.
Daye, M., Klepac-Ceraj, V., Pajusalu, M., Rowland, S., Farrell-Sherman, A., Beukes, N., Tamura, N., Fournier, G., Bosak, T., 2019. Light-driven anaerobic microbial oxidation of manganese. Nature 576, 311-314.
De Yoreo, J.J., Vekilov, P.G., 2003. Principles of Crystal Nucleation and Growth. Rev. Mineral. Geochem. 54, 57-93.
Diem, D., Stumm, W., 1984. Is dissolved Mn^{2+} being oxidized by O_2 in absence of Mn-bacteria or surface catalysts? Geochim. Cosmochim. Acta 48, 1571-1573.
Droz, B., Dumas, N., Duckworth, O.W., Peña, J., 2015. A Comparison of the Sorption Reactivity of Bacteriogenic and Mycogenic Mn Oxide Nanoparticles. Environ. Sci. Technol. 49, 4200-4208.
Eitel, E.M., Zhao, S., Tang, Y., Taillefert, M., 2018. Effect of manganese oxide aging and structure transformation on the kinetics of thiol oxidation. Environ. Sci. Technol. 52, 13202-13211.
Feng, X., Zhao, H., Liu, F., Cui, H., Tan, W., Li, W., 2015. Transformation from Phyllomanganates to Todorokite under Various Conditions: A Review of Implication for Formation Pathway of Natural Todorokite. Advances in the Environmental Biogeochemistry of Manganese Oxides. American Chemical Society, pp. 107-134.
Ferris, F.G., Phoenix, V., Fujita, Y., Smith, R.W., 2004. Kinetics of calcite precipitation induced by ureolytic bacteria at 10 to 20°C in artificial groundwater. Geochim. Cosmochim. Acta 68, 1701-1710.
Fortunato, J., Peña, J., Benkaddour, S., Zhang, H., Huang, J., Zhu, M., Logan, B.E., Gorski, C.A., 2020. Surveying Manganese Oxides as Electrode Materials for Harnessing Salinity Gradient Energy. Environ. Sci. Technol. 54, 5746-5754.
Gao, Z., Liu, J., Skurie, C., Zhu, Y., Jun, Y.-S., 2022. Photochemical reactions of dissolved organic matter and bromide ions facilitate abiotic formation of manganese oxide solids. Water Res., 118831.
Gillispie, E.C., Austin, R.E., Rivera, N.A., Bolich, R., Duckworth, O.W., Bradley, P., Amoozegar, A., Hesterberg, D., Polizzotto, M.L., 2016. Soil Weathering as an Engine for Manganese Contamination of Well Water. Environ. Sci. Technol. 50, 9963-9971.
Grebel, J.E., Charbonnet, J.A., Sedlak, D.L., 2016. Oxidation of organic contaminants by manganese oxide geomedia for passive urban stormwater treatment systems. Water Res. 88, 481-491.

Hjorth, T., 2004. Effects of freeze-drying on partitioning patterns of major elements and trace metals in lake sediments. Anal. Chim. Acta 526, 95-102.
Huang, J., Zhang, H., 2019. Mn-based catalysts for sulfate radical-based advanced oxidation processes: A review. Environ. Int. 133, 105141.
Johnson, J.E., Savalia, P., Davis, R., Kocar, B.D., Webb, S.M., Nealson, K.H., Fischer, W.W., 2016. Real-Time Manganese Phase Dynamics during Biological and Abiotic Manganese Oxide Reduction. Environ. Sci. Technol. 50, 4248-4258.
Jun, Y.-S., Martin, S.T., 2003. Microscopic observations of reductive manganite dissolution under oxic conditions. Environ. Sci. Technol. 37, 2363-2370.
Jung, H., Chadha, T., Kim, D., Biswas, P., Jun, Y.-S., 2017. Photochemically-assisted Fast Abiotic Oxidation of Manganese and Formation of δ–MnO_2 Nanosheets in Nitrate Solution. Chem. Commun. 53, 4445-4448.
Jung, H., Taillefert, M., Sun, J., Wang, Q., Borkiewicz, O.J., Liu, P., Yang, L., Chen, S., Chen, H., Tang, Y., 2020. Redox Cycling Driven Transformation of Layered Manganese Oxides to Tunnel Structures. J. Am. Chem. Soc. 142, 2506-2513.
Jung, H., Xu, X., Wan, B., Wang, Q., Borkiewicz, O.J., Li, Y., Chen, H., Lu, A., Tang, Y., 2021. Photocatalytic oxidation of dissolved Mn(II) on natural iron oxide minerals. Geochim. Cosmochim. Acta 312, 343-356.
Junta, J.L., Hochella Jr, M.F., 1994. Manganese (II) oxidation at mineral surfaces: A microscopic and spectroscopic study. Geochim. Cosmochim. Acta 58, 4985-4999.
Knocke, W.R., Hoehn, R.C., Sinsabaugh, R.L., 1987. Using Alternative Oxidants to Remove Dissolved Manganese From Waters Laden With Organics. Journal (American Water Works Association) 79, 75-79.
Knocke, W.R., Occiano, S.C., Hungate, R., 1991. Removal of Soluble Manganese by Oxide-coated Filter Media: Sorption Rate and Removal Mechanism Issues. Journal (American Water Works Association) 83, 64-69.
Knocke, W.R., Ramon, J.R., Thompson, C.P., 1988. Soluble Manganese Removal on Oxide-Coated Filter Media. Journal (American Water Works Association) 80, 65-70.
Learman, D., Voelker, B., Vazquez-Rodriguez, A., Hansel, C., 2011. Formation of manganese oxides by bacterially generated superoxide. Nat. Geosci. 4, 95-98.
Lee, S., Xu, H., 2016. XRD and TEM studies on nanophase manganese oxides in freshwater ferromanganese nodules from Green Bay, Lake Michigan. Clays Clay Miner. 64, 523-536.
Li, J., Zhao, L., Huang, C.-H., Zhang, H., Zhang, R., Elahi, S., Sun, P., 2020. Significant Effect of Evaporation Process on the Reaction of Sulfamethoxazole with Manganese Oxide. Environ. Sci. Technol. 54, 4856-4864.
Liu, W., Hao, J., Elzinga, E.J., Piotrowiak, P., Nanda, V., Yee, N., Falkowski, P.G., 2020. Anoxic photogeochemical oxidation of manganese carbonate yields manganese oxide. Proc. Natl. Acad. Sci. 117, 22698-22704.
Madden, A.S., Hochella, M.F., 2005. A test of geochemical reactivity as a function of mineral size: Manganese oxidation promoted by hematite nanoparticles. Geochim. Cosmochim. Acta 69, 389-398.
Madison, A.S., Tebo, B.M., Luther, G.W., 3rd, 2011. Simultaneous determination of soluble manganese(III), manganese(II) and total manganese in natural (pore)waters. Talanta 84, 374-381.
Madison, A.S., Tebo, B.M., Mucci, A., Sundby, B., Luther, G.W., 2013. Abundant porewater Mn (III) is a major component of the sedimentary redox system. Science 341, 875-878.
Miyata, N., Tani, Y., Sakata, M., Iwahori, K., 2007. Microbial manganese oxide formation and interaction with toxic metal ions. J. Biosci. Bioeng. 104, 1-8.

533 Montserrat, F., Renforth, P., Hartmann, J., Leermakers, M., Knops, P., Meysman, F.J., 2017.
534 Olivine Dissolution in Seawater: Implications for CO2 Sequestration through Enhanced
535 Weathering in Coastal Environments. Environ. Sci. Technol. 51, 3960-3972.
536 Morgan, J.J., 2005. Kinetics of reaction between O_2 and Mn (II) species in aqueous solutions.
537 Geochim. Cosmochim. Acta 69, 35-48.
538 Morgan, J.J., Schlautman, M.A., Bilinski, H., 2021. Rates of Abiotic MnII Oxidation by O2:
539 Influence of Various Multidentate Ligands at High pH. Environ. Sci. Technol. 55, 14426-14435.
540 Nealson, K.H., Tebo, B.M., Rosson, R.A., 1988. Occurrence and mechanisms of microbial
541 oxidation of manganese. Advances in Applied Microbiology ADAMAP 33.
542 Nico, P.S., Anastasio, C., Zasoski, R.J., 2002. Rapid photo-oxidation of Mn (II) mediated by
543 humic substances. Geochim. Cosmochim. Acta 66, 4047-4056.
544 Oldham, V.E., Mucci, A., Tebo, B.M., Luther Iii, G.W., 2016. Soluble Mn(III)-L complexes are
545 abundant in oxygenated waters and stabilized by humic ligands. Geochim. Cosmochim. Acta
546 199.
547 Planavsky, N.J., Asael, D., Hofmann, A., Reinhard, C.T., Lalonde, S.V., Knudsen, A., Wang,
548 X., Ossa Ossa, F., Pecoits, E., Smith, A.J.B., Beukes, N.J., Bekker, A., Johnson, T.M.,
549 Konhauser, K.O., Lyons, T.W., Rouxel, O.J., 2014. Evidence for oxygenic photosynthesis half
550 a billion years before the Great Oxidation Event. Nat. Geosci. 7, 283-286.
551 Post, J.E., 1999. Manganese oxide minerals: Crystal structures and economic and
552 environmental significance. Proc. Natl. Acad. Sci. 96, 3447-3454.
553 Reinhard, C.T., Raiswell, R., Scott, C., Anbar, A.D., Lyons, T.W., 2009. A Late Archean
554 Sulfidic Sea Stimulated by Early Oxidative Weathering of the Continents. Science 326, 713-
555 716.
556 Spiro, T.G., Bargar, J.R., Sposito, G., Tebo, B.M., 2009. Bacteriogenic manganese oxides. Acc.
557 Chem. Res. 43, 2-9.
558 Sung, W., Morgan, J.J., 1981. Oxidative removal of Mn (II) from solution catalysed by the γ-
559 FeOOH (lepidocrocite) surface. Geochim. Cosmochim. Acta 45, 2377-2383.
560 Tang, X., Xie, B., Chen, R., Wang, J., Huang, K., Zhu, X., Li, G., Liang, H., 2020. Gravity-
561 driven membrane filtration treating manganese-contaminated surface water: Flux stabilization
562 and removal performance. Chem. Eng. J. 397, 125248.
563 Tebo, B.M., Clement, B.G., Dick, G.J.J.M.o.e.m., 2007. Biotransformations of manganese.
564 1223-1238.
565 Tebo, B.M., Johnson, H.A., McCarthy, J.K., Templeton, A.S., 2005. Geomicrobiology of
566 manganese(II) oxidation. Trends Microbiol. 13, 421-428.
567 Toyoda, K., Tebo, B.M., 2016. Kinetics of Mn(II) oxidation by spores of the marine Bacillus
568 sp. SG-1. Geochim. Cosmochim. Acta 189, 58-69.
569 Turner, S., Post, J.E., 1988. Refinement of the substructure and superstructure of romanechite.
570 Am. Mineral. 73, 1155-1161.
571 Von Langen, P.J., Johnson, K.S., Coale, K.H., Elrod, V.A., 1997. Oxidation kinetics of
572 manganese (II) in seawater at nanomolar concentrations. Geochim. Cosmochim. Acta 61,
573 4945-4954.
574 Wang, Y., Bai, Y., Su, J., Ali, A., Gao, Z., Huang, T., Cao, M., Ren, M., 2023. Advances in
575 microbially mediated manganese redox cycling coupled with nitrogen removal in wastewater
576 treatment: A critical review and bibliometric analysis. Chem. Eng. J. 461, 141878.
577 Wang, Z., Tebo, B.M., Giammar, D.E., 2014. Effects of Mn (II) on UO_2 Dissolution under
578 Anoxic and Oxic Conditions. Environ. Sci. Technol. 48, 5546–5554.
579 Webb, S., Fuller, C., Tebo, B., Bargar, J., 2006. Determination of uranyl incorporation into
580 biogenic manganese oxides using X-ray absorption spectroscopy and scattering. Environ. Sci.
581 Technol. 40, 771-777.

582 Wehrli, B., Friedl, G., Manceau, A., 1995. Reaction rates and products of manganese oxidation
583 at the sediment-water interface. in: Huang, C.P., Omelia, C.R., Morgan, J.J. (Eds.). Aquatic
584 Chemistry: Interfacial and Interspecies Processes. American Chemical Society, pp. 111-134.
585 Yang, J., Xu, J.J., 2003. Influence of synthesis conditions on the electrochemical properties of
586 nanostructured amorphous manganese oxide cryogels. J. Power Sources 122, 181-187.
587 Yuan, Y., Liu, C., Byles, B.W., Yao, W., Song, B., Cheng, M., Huang, Z., Amine, K.,
588 Pomerantseva, E., Shahbazian-Yassar, R., Lu, J., 2019. Ordering Heterogeneity of [MnO6]
589 Octahedra in Tunnel-Structured MnO2 and Its Influence on Ion Storage. Joule 3, 471-484.
590 Zhang, T., Liu, L., Tan, W., Suib, S.L., Qiu, G., Liu, F., 2018. Photochemical Formation and
591 Transformation of Birnessite: Effects of Cations on Micromorphology and Crystal Structure.
592 Environ. Sci. Technol. 52, 6864-6871.
593
594

595 **Figures**

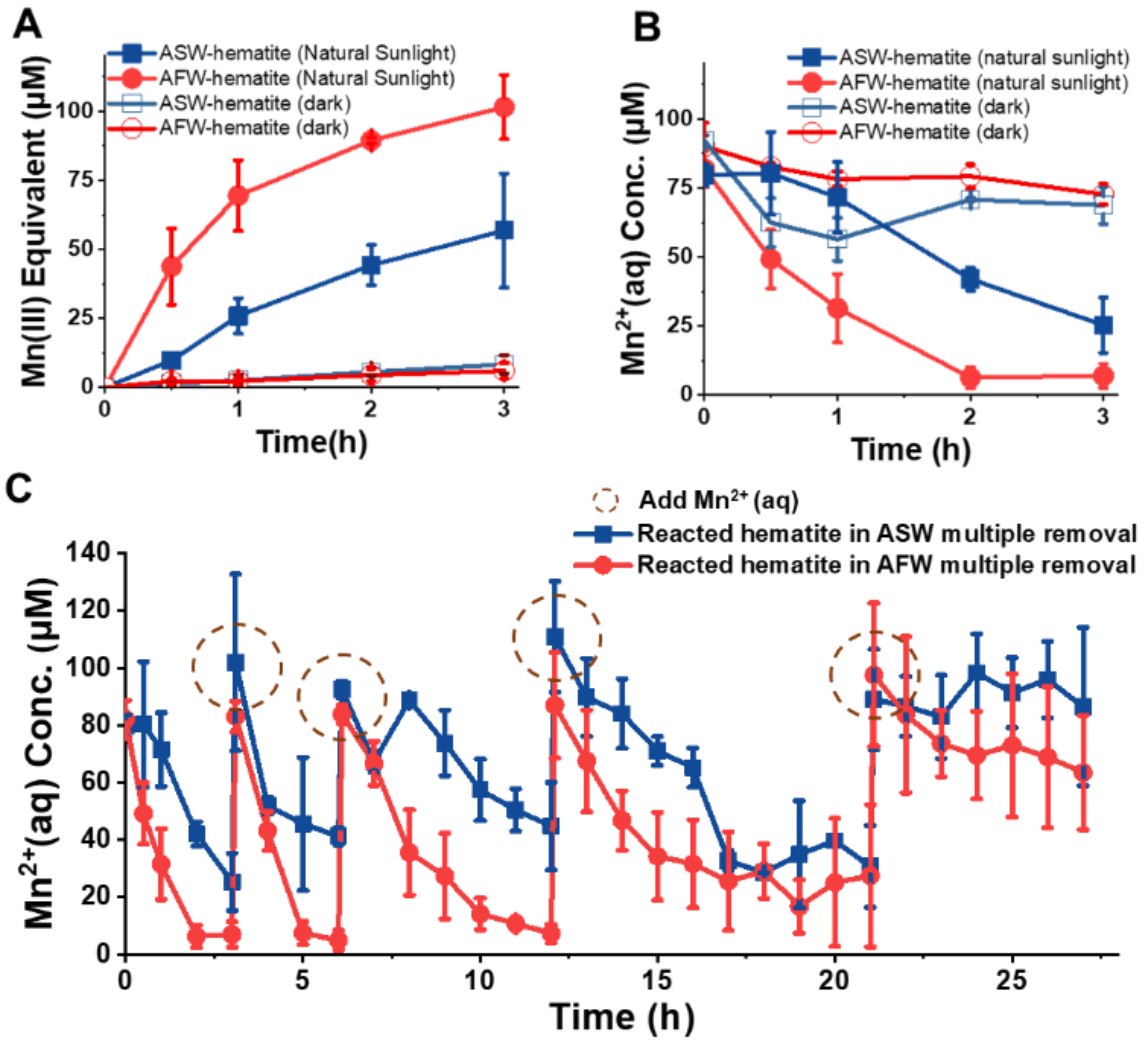

596

597 **Fig. 1.** Natural sunlight-mediated rapid photocatalytic oxidation of Mn^{2+}(aq) by hematite. (A)
598 The increase of oxidized Mn^{2+}(aq) expressed as Mn(III) equivalent. (B) The decrease of
599 Mn^{2+}(aq) concentration. (C) Dynamics of Mn^{2+}(aq) concentration during multiple addition of
600 100 μM Mn^{2+}(aq).

601

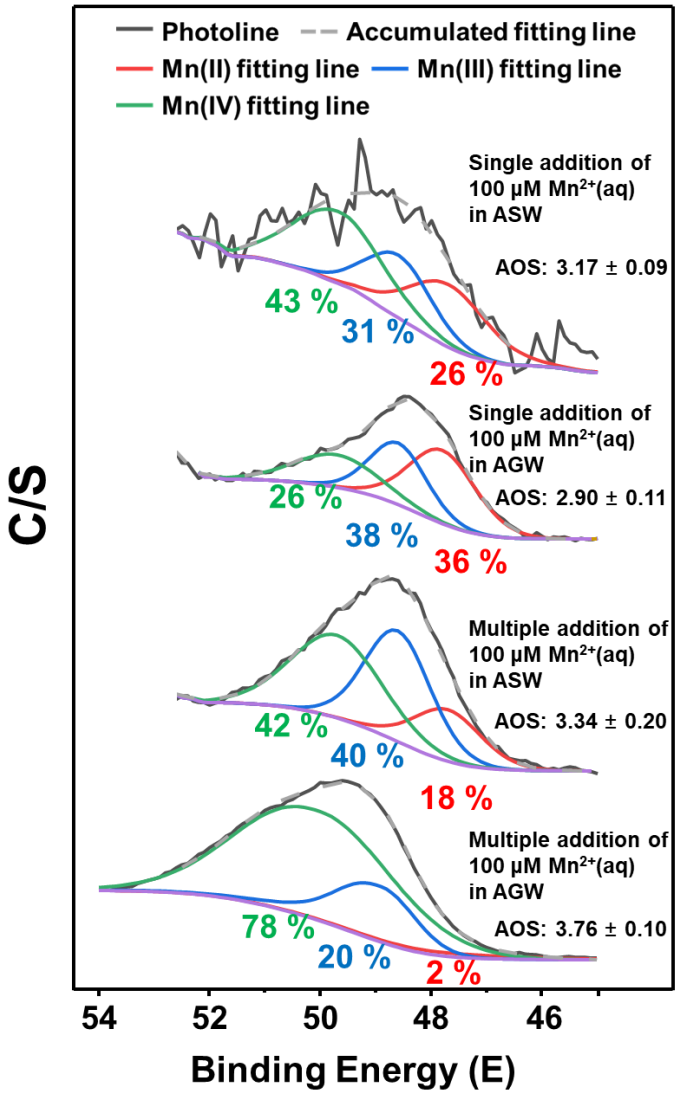

Fig. 2. XPS Mn 3p analysis of the photocatalytically produced Mn oxides on hematite. In the ASW-hematite suspension, the photocatalytically formed Mn oxides with single and multiple addition of 100 μM Mn^{2+}(aq) showed consistent average oxidation states (AOS) of Mn oxides of around 3.1–3.2. However, in the AFW-hematite suspension, the AOS of Mn oxides produced with multiple addition of 100 μM Mn^{2+}(aq) is much higher (AOS 3.73) than that with single addition of 100 μM Mn^{2+}(aq) (AOS 2.8).

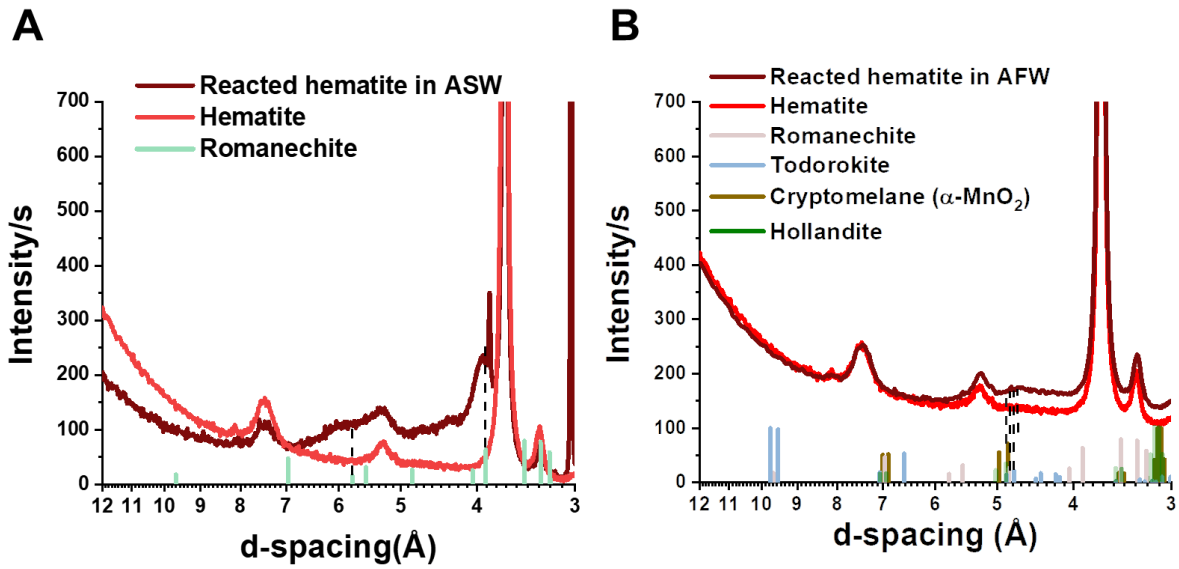

610

611 **Fig. 3.** Synchrotron XRD analysis of Mn oxides produced in the ASW-hematite (A) and AFW-

612 hematite (B) suspensions.

613

614

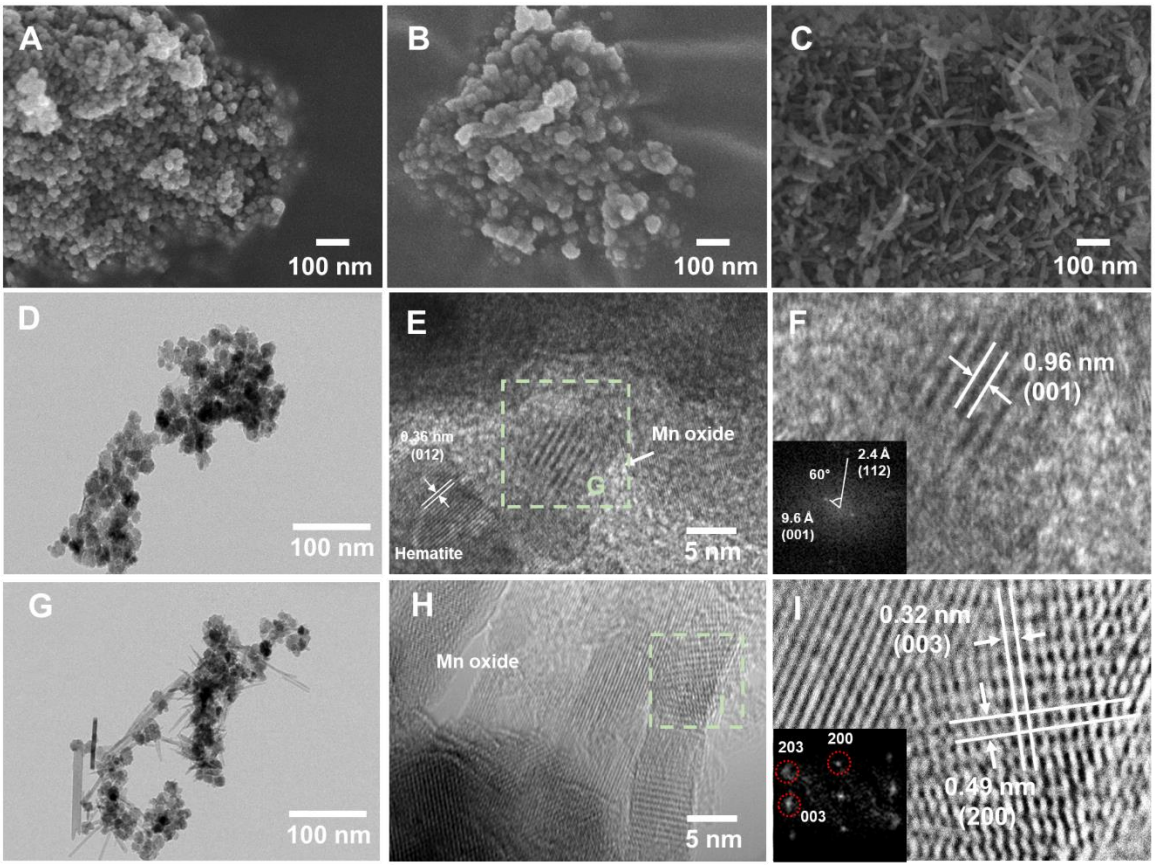

615

616 **Fig. 4.** SEM and TEM analyses of the Mn oxides. SEM images of (A) pristine hematite
617 nanoparticles, (B) Mn oxides on hematite in the ASW-hematite suspension, and (C) Mn oxides
618 on hematite in the AFW-hematite suspension. (D–F) TEM images of nucleated Mn oxides on
619 hematite in the ASW-hematite suspension. (G–I) TEM images of nucleated Mn oxides on
620 hematite in the AFW-hematite suspension.

621

622

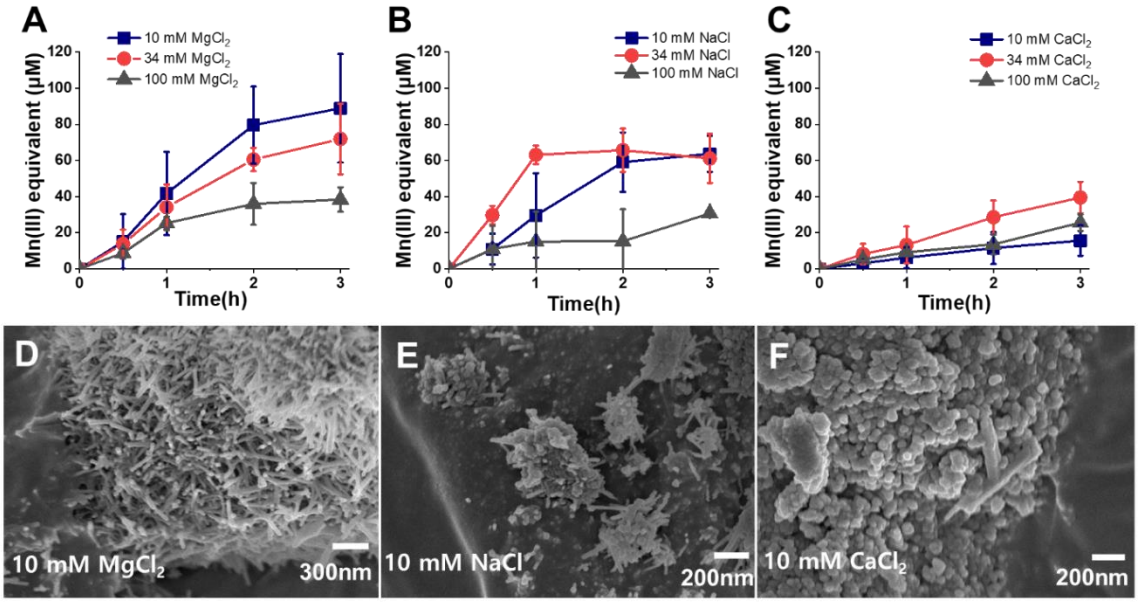

623

624 **Fig. 5.** Effect of cation species (Mg^{2+}, Na^{+}, and Ca^{2+}) and concentration on the Mn^{2+}(aq)

625 oxidation rates (A–C) and morphology the Mn oxides (D–F) analyzed by SEM.

626

627

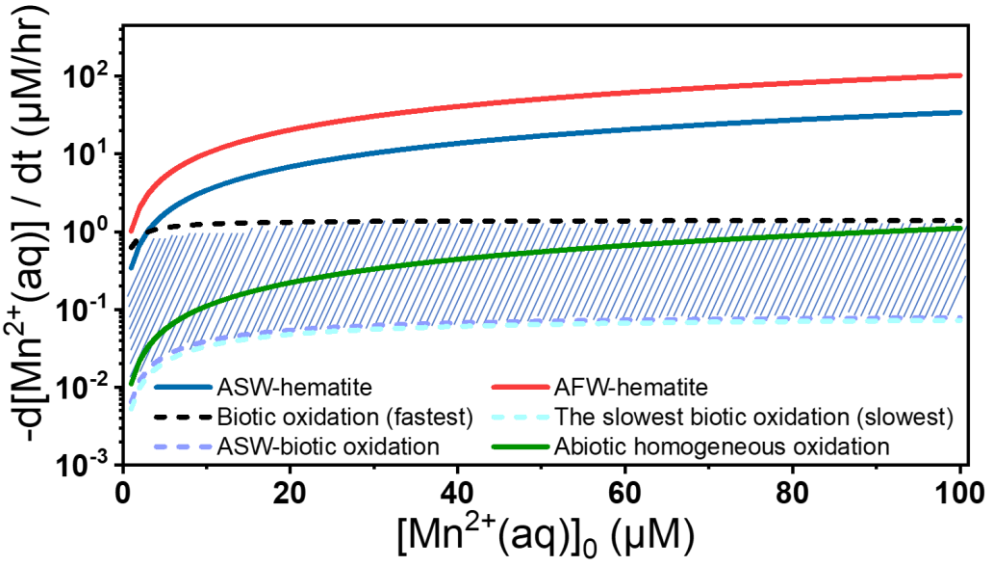

628

629 **Fig. 6.** Comparison of Mn^{2+}(aq) oxidation rates by photocatalytic oxidation in this study with
630 abiotic oxidation by dissolved oxygen and microbial oxidation by the marine Bacillus sp. SG-
631 1 as a function of the initial concentration of Mn^{2+}(aq) at pH ~8.